ACS OMEGA

Open Access

http://pubs.acs.org/journal/acsodf

Article

In Situ Electrochemical Conversion of Biomass-Derived 5-Hydroxymethylfurfural into 2,5-Furandicarboxylic Acid by Time-Controlled Aerosol-Assisted Chemical Vapor Deposited FeNi Catalyst

Muthumariappan Akilarasan, Muhammad Ali Ehsan, Muhammad Nawaz Tahir, Mudasir Akbar Shah, Wasif Farooq,* and Jerome Morris Princey

Cite This: *ACS Omega* 2024, 9, 42766−42777

Read Online

ACCESS | Metrics & More | Article Recommendations | Supporting Information

ABSTRACT: The conversion of 5-hydroxymethylfurfural (HMF) into valuable chemicals, such as 2,5-furandicarboxylic acid (FDCA), is pivotal for sustainable chemical production, offering a renewable pathway to biodegradable plastics and high-value organic compounds. This pioneering study explores the synthesis of FeNi nanostructures via aerosol-assisted chemical vapor deposition (AACVD) for the electrochemical oxidation of HMF to FDCA. By adjusting the deposition time, we developed two distinct nanostructures: FeNi-40, which features nanowires with spherical terminations, and FeNi-80, which features aggregated spherical structures. X-ray diffraction (XRD) confirmed that both nanostructures possess a phase-pure face-centered cubic (FCC) crystal structure. Electrochemical tests conducted using FeNi nanocatalysts on Ni foam revealed that FeNi-40 requires a significantly lower onset potential for HMF oxidation (1.32 V vs RHE) compared to FeNi-80 (1.40 V vs RHE). This difference is attributed to the unique nanowire morphology of FeNi-40, which provides a higher density of active sites and a larger electrochemically active surface area, thereby enhancing the efficiency of the electrochemical process. When tested in an H-type electrolyzer with a Nafion membrane, FeNi-40 demonstrated a remarkable Faradaic efficiency of 96.42% and a high product yield, underscoring the potential of morphology-controlled FeNi nanostructures to enhance the efficiency of sustainable electrochemical processes significantly.

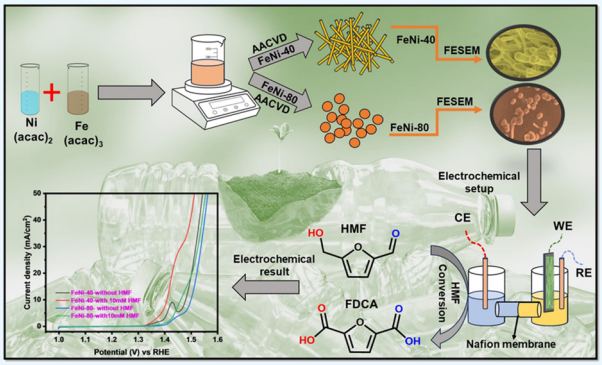

INTRODUCTION

The quest for sustainable energy sources has intensified in response to global climate change and environmental degradation concerns.[1] Furthermore, over-relying on nonrenewable fossil resources poses multifaceted challenges to eco-sustainability.[2,3] Environmental degradation, carbon emissions, and geopolitical tensions associated with fossil fuel extraction underscore the urgent need for alternative green, environmentally friendly, and renewable energy.[4,5] Scientists are developing renewable alternatives to address this challenge sustainably, with lignocellulosic biomass emerging as a promising option.[6,7] 5-Hydroxymethylfurfural (HMF) is a promising candidate among the various biomass-derived molecules.[8] HMF can be converted to several valuable chemicals such as levulinic acid, 5-hydroxymethyl-2-furancarboxylic acid (HMFCA), 2,5-diformylfuran (DFF), 5-formyl-2-furancarboxylic acid (FFCA), and formic acid. These chemicals are critical in producing fine chemicals and pharmaceuticals, adding significant value to biomass conversion processes. Among these HMF conversion products, 2,5-furandicarboxylic acid (FDCA) is highly prized as an oxidation product because of its frequent role as a precursor for producing biopolymer poly(ethylene furanoate) (PEF).[9] Compared to petroleum-derived terephthalic acid (TPA) used in poly(ethylene terephthalate) (PET) production, biobased PEF offers distinct advantages such as superior gas barrier performance, recyclability, and enhanced mechanical properties. FDCA, as a precursor to bioplastics, polyester resins, and other high-value materials, has significant potential to replace traditional petrochemical-derived counterparts.[10,11] However, the traditional chemical methods for converting HMF to valuable chemicals present their own challenges, such as low selectivity,

Received: May 5, 2024
Revised: October 8, 2024
Accepted: October 8, 2024
Published: October 14, 2024

harsh reaction conditions, and the generation of undesirable byproducts.[12,13]

In this context, electrochemical methods have garnered significant attention as a cleaner, more sustainable approach to HMF conversion to valuables.[14] Electrochemical processes offer several distinct advantages over conventional chemical methods.[15,16] They can operate under mild reaction conditions and minimize the environmental impact. Moreover, electrochemical reactions can be finely tuned to achieve high selectivity and yield, thus overcoming the limitations of the traditional catalytic approaches. Furthermore, electrochemical oxidation that takes place at ambient pressure and temperature can be coupled with electrochemical reduction; electrons obtained at the anode during HMF oxidation can be used concurrently for the reduction of proton at the cathode, leading to the formation of green H_2 fuel, which significantly increases the worth of this approach.[17]

The electrochemical oxidation of HMF using noble metal catalysts, such as Pd, Pt, Au, and Ru, demonstrates a low onset potential for HMF oxidation. However, they typically yield extremely low current densities across the applied potential range.[17] In addition, the cost of noble metals poses a challenge for their commercialization. To address these challenges, research has increasingly focused on developing catalysts made from more abundant and cost-effective elements such as iron (Fe) and nickel (Ni), cobalt (Co), and manganese (Mn). In addition, recent studies highlight the potential of trimetallic and bimetallic catalysts for the oxygen evolution reaction (OER) and 5-hydroxymethylfurfural oxidation reaction (HMFOR). For instance, Zhang et al. have developed a method for the one-step synthesis of trimetallic NiCoFe-layered double hydroxide (NiCoFe-LDH) nanosheets with a thickness of 1.36 nm. These nanosheets exhibit an overpotential of 330 mV at 10 mA cm^{-2} for the OER and a Tafel slope of 68 mV dec^{-1}.[18] Similarly, Liu et al. designed NiCoMn-layered double hydroxide (NiCoMn-LDH) nanosheets, achieving an overpotential of 370 mV at 50 mA cm^{-2} and a Tafel slope of 118 mV dec^{-1}.[19] Moreover, You et al. prepared three-dimensional (3D) Ni_2P nanoparticle arrays on nickel foam (Ni_2P NPA/NF), which displayed a low onset potential of 1.43 V vs reversible hydrogen electrode (RHE) for HMF oxidation and achieved a 100% Faradaic efficiency (FE).[20] Another significant development by Wang et al. involved Ni nanoparticles that attained a remarkable 99.8% HMF conversion and a 99.2% FDCA yield at 1.36 V.[21] Ge et al. also reported on single-atom ruthenium on nickel oxide (Ru_1-NiO) as an efficient catalyst, operating at a low potential of 1.283 V vs RHE at 10 mA cm^{-2}.[22] Finally, Zheng et al. developed Cu nanowire arrays modified with nickel−cobalt layered double hydroxide nanosheets (NiCoNSs/CuNWs) for HMF oxidation, achieving 10 mA cm^{-2} at 1.44 V vs RHE, with a Tafel slope of 97.2 mV dec^{-1}.[23] Within the various bimetallic alloys, the combination of Fe and Ni alloys has garnered significant interest due to their unfilled d orbitals, which enhance catalytic activity.[24] The synergistic effect between Fe and Ni arises from the modification of Ni electronic structure by neighboring Fe atoms, leading to improved catalytic performance.[25] Additionally, the natural abundance, environmental compatibility, and high electrical conductivity of Fe and Ni make them attractive candidates for sustainable catalyst design.[26,27] In addition, alloying Ni with Fe will provide a continuous supply of clean and active interfaces for HMF molecules, resulting in improved catalytic performance.[18,28,29] However, the catalytic performance of FeNi alloys is strongly influenced by their morphological characteristics, emphasizing the importance of understanding structure−property relationships in catalyst design.[25,,31]

FeNi has been prepared through chemical (hydrothermal synthesis,[32] solvothermal synthesis[33]) and physical (PVD,[34] ball milling[35]) methodologies. Each method offers unique advantages for the preparation of nanostructured materials. However, they may also suffer from drawbacks, such as longer processing times, limited scalability, challenges in achieving uniformity, and higher complexity. To date, the aerosol-assisted chemical vapor deposition (AACVD) method offers distinct advantages in synthesizing multimetallic alloys. This technique allows precise control over the deposition process, enabling the fabrication of nanostructured materials with tailored morphologies and compositions.[36,37] AACVD is a scalable and cost-effective synthesis approach, making it suitable for the large-scale production of FeNi catalysts for industrial applications.

In this contribution, we synthesized a FeNi electrocatalyst with different morphologies using AACVD. We investigated the electrochemical conversion of HMF to FDCA with a high conversion efficiency of 96.42% and a high yield of 95.32%. The morphology was controlled by different deposition times of 40 and 80 min and monitored using scanning electron microscopy (SEM). The catalysts were tested for the OER and HMF oxidation reaction (HMFOR). The results revealed that FeNi-40 exhibited a significantly lower onset potential of 1.32 V vs RHE for HMF oxidation than FeNi-80 1.40 V vs RHE. These findings underscore the superior catalytic activity of FeNi-40 in HMF oxidation, highlighting its potential in biomass conversion processes.

MATERIALS AND METHODS

Chemicals and Reagents. Iron(III) acetylacetonate ($Fe(acac)_3$) and nickel(II) acetylacetonate ($Ni(acca)_2$) were purchased from Sigma-Aldrich. Nickel foam, with a thickness of 1.6 mm and 110% porosity, was obtained from Goodfellow Cambridge Ltd. Furthermore, 5-hydroxymethylfurancarboxylic acid (HMFCA, 98%) was purchased from Sisco Research Laboratory Pvt. Ltd., India. On the contrary, 2,5-furandicarboxylic acid (FDCA) was acquired from Biosynth Reagents Ltd. KOH (85%, Sigma-Aldrich) was used without further purification. Deionized water (Barnstead E-pure water purification system, resistivity >18 MΩ cm) was used to prepare the HMF solutions and electrolytes.

Materials Instrumentation. The morphological analysis of the synthesized catalysts was performed using a FESEM-JEOL-7600F instrument equipped with an energy-dispersive X-ray (EDX) spectrometer and elemental mapping. This high-resolution scanning electron microscope allowed for detailed imaging of the catalyst surfaces, providing insights into their nanostructures and morphologies. The catalyst's crystalline structure and phase composition were analyzed using an XPERT-PRO XRD (PANalytical B.V.). This instrument utilized XRD to characterize the sample's crystallographic properties, including identifying phases and determining crystallographic parameters. X-ray photoelectron spectroscopy (XPS) was analyzed with Thermo ESCALAB 250.

Electrochemical Measurements. Electrochemical measurements were performed at room temperature using a Gamry Potentiostat (Interface 1010E). The standard three-electrode setup included a nickel foam working electrode, a platinum

https://doi.org/10.1021/acsomega.4c04274
ACS Omega 2024, 9, 42766−42777

Scheme 1. Schematic Representation of the Synthesis of the FeNi Nanoalloy Using the AACVD Method

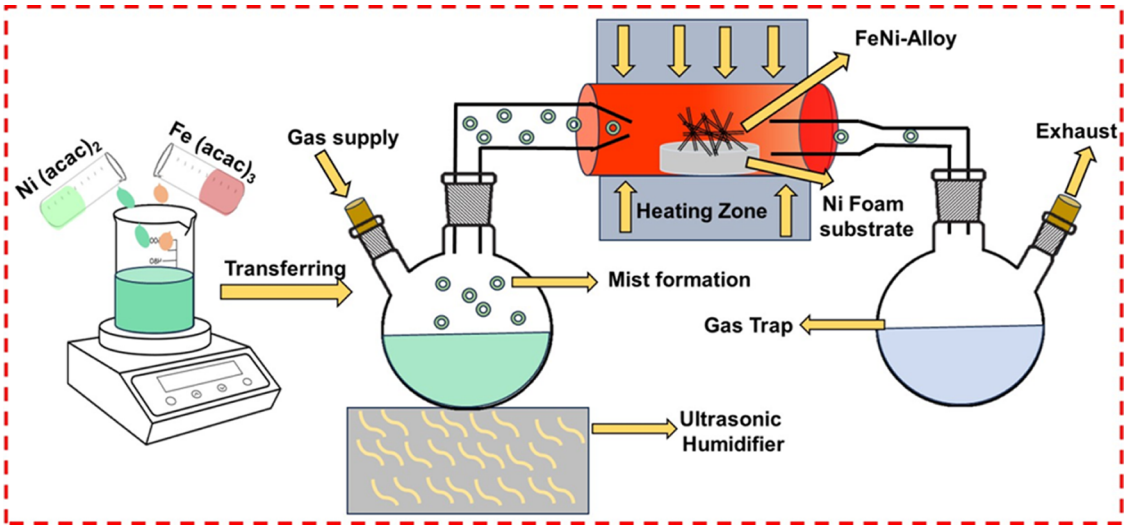

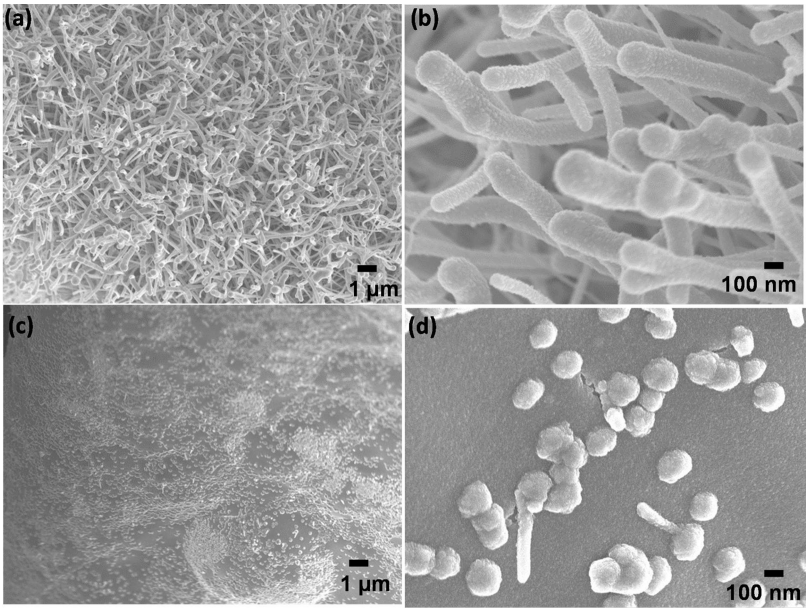

Figure 1. (a) FESEM images of FeNi-40: (a) overview FESEM image showing uniformly grown FeNi nanowires, (b) high-resolution FESEM indicating spherical head termination, (c) overview SEM image for sample FeNi-80 showing a compact film with spherical nanostructures, and (d) high-resolution FESEM indicating spherical nanostructures onto the FeNi film.

wire counter electrode, and a Hg/HgO (filled with 1.0 M KOH) reference electrode. In addition, electrochemical measurements were carried out using an H-cell setup, with compartments separated by a Nafion 115 (with a thickness of 0.127 mm) cation exchange membrane. In contrast, other electrochemical studies were performed in a single-cell chamber. The nickel foam (dimensions of 1 × 1 cm, with a thickness of 1.6 mm and a porosity of 110 ppi) was subjected to a surface treatment procedure: it was initially washed in 3 M HCl for 30 min to eliminate surface oxides, followed by ultrasonication in ethanol and acetone for 30 min each. A 1.0 M KOH solution served as the supporting electrolyte. Linear sweep voltammetry (LSV) was used to assess the activity of the OER and HMFOR in a 1 M KOH solution with a pH of approximately 13.64. The LSV curves were recorded at a scanning rate of 5 mV s^{-1}. The HMFOR experiments used a concentration of 10 mM HMF. All of the electrochemical studies in this report were performed without *iR* compensation. The potentials were calibrated using the reversible hydrogen electrode (RHE) based on eq 1

$$\mathrm{RHE} = E(\mathrm{Hg/HgO}) + 0.059\,\mathrm{pH} + 0.105\ \mathrm{V} \quad (1)$$

High-Performance Liquid Chromatography (HPLC) Measurements. HPLC analysis was performed using a Shimadzu Prominence LC-2030C system with an ultraviolet−visible detector. The sample (~500 μL) was withdrawn during potentiostatic electrolysis using a 1.0 mL glass syringe, diluted to 1.5 mL with ultrapure water, and analyzed using HPLC. The parameters were set as follows: the UV detector operated at a wavelength of 265 nm, while the mobile phase consisted of methanol (phase A) and a 5 mM ammonium formate aqueous solution (phase B) in a ratio of 3:7. The flow rate remained constant at 0.6 mL/min. Separation was achieved using a 4.6 mm × 150 mm Shim-pack GWS 5 μm

https://doi.org/10.1021/acsomega.4c04274
ACS Omega 2024, 9, 42766−42777

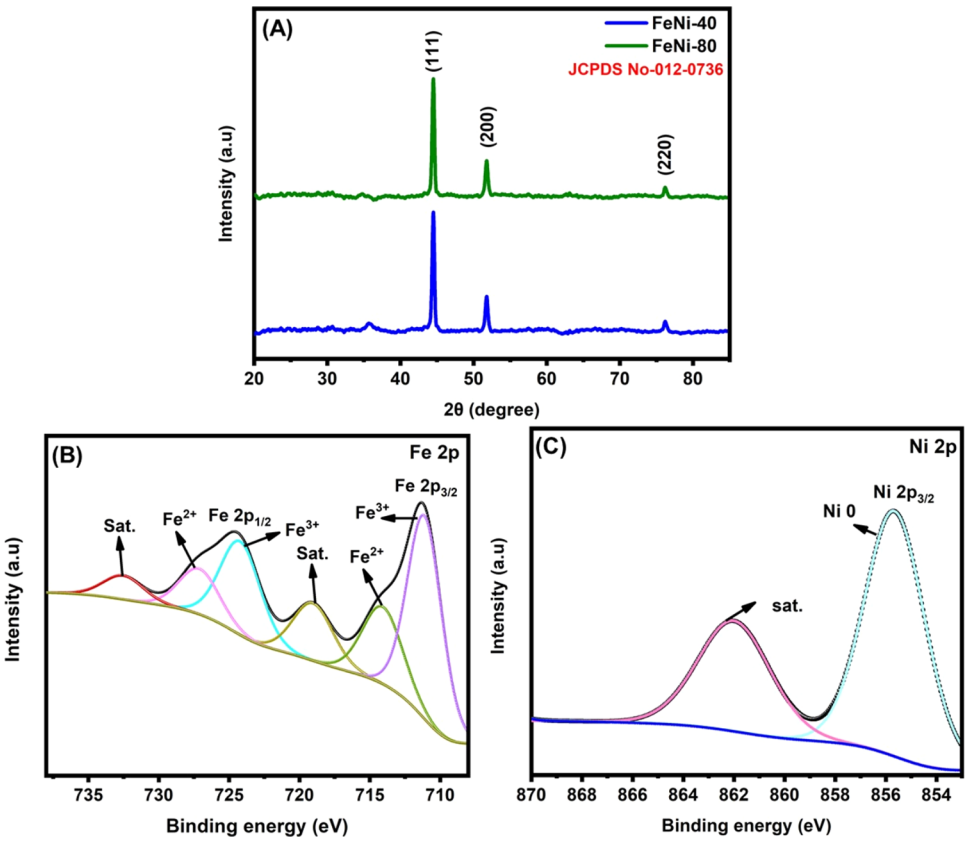

Figure 2. XRD pattern of the FeNi alloy reveals signals attributed to the planes (111), (200), and (220) within the FCC cubic crystal structure, indicating its distinct structural composition. (B) XPS spectrum of Fe 2p, showing distinct peaks corresponding to Fe^{2+} and Fe^{3+} oxidation states, indicating the presence of both Fe(II) and Fe(III) species within the FeNi nanostructures. (C) XPS spectrum of Ni 2p, featuring a prominent peak for metallic Ni (Ni^0) and smaller contributions from Ni^{2+}, confirming the alloy's composition and oxidation state distribution.

C18 column, with each separation run lasting for approximately 7 min. This analytical methodology enabled the accurate identification and quantification of HMF oxidation products, providing valuable information about the electrochemical conversion process. The standard calibration curves for HMF, FDCA, and HMFCA are given in Figure S2.

Synthesis of FeNi/NF. Fe−Ni alloy nanostructures were synthesized through the AACVD method, employing Ni Foam as the substrate for FeNi deposition. At first, iron(III) acetylacetonate ($Fe(acac)_3$) and nickel(II) acetylacetonate ($Ni(acac)_2$) were mixed in a 1:1 ratio, corresponding to 0.5 mmol each. These precursors were dissolved in 15 mL of methanol under stirring to ensure homogeneity. The mixed metal precursors were subjected to ultrasonic humidification to generate an aerosol mist. This process helps to facilitate the efficient transfer of precursors to the reaction chamber. The aerosol mist containing the metal precursors was introduced into a preheated tube furnace at approximately 475 °C. A carrier gas mixture consisting of 10% H_2 and 90% N_2 was used to facilitate the transport and decomposition of precursors. Ni foam inside the tube furnace received the decomposed metal precursors, where the chemical vapor deposition (CVD) process occurred. The deposition was carried out for two different durations: 40 and 80 min, resulting in samples labeled FeNi-40 and FeNi-80, respectively. Upon completion of the deposition, the aerosol supply was terminated, and 100% H_2 gas was passed over the catalyst to ensure the formation of FeNi alloy. This step helps reduce any residual precursors and promotes alloy formation. The amount of FeNi deposited on the Ni Foam substrates was measured before and after deposition using the appropriate analytical techniques. For FeNi-40, the deposition mass was found to be 24 μg, while for FeNi-80, it was 37 μg, indicating the variation in the deposition mass with the deposition time. The graphical form of synthesis of FeNi alloys is displayed in Scheme 1.

RESULTS AND DISCUSSION

Morphological and XRD Analysis. Field emission scanning electron microscopy (FESEM) was employed to analyze the morphologies of the prepared FeNi-40 and FeNi-80 samples. Figure 1a,b show the FeNi-40 FESEM images at different magnifications of 1 μm (overview) and 100 nm (high-resolution SEM). At a magnification of 1 μm, FeNi-40 exhibits a well-defined, uniform size and regular arrangement of nanowires throughout the substrate (Figure 1a). Upon further magnification to 100 nm, a spherical head formation can be observed at the termination points of the nanowires (Figure 1b). Conversely, Figure 1c,d FESEM images of FeNi-80 at various magnifications revealed a contrasting morphology, i.e., the formation of a compact film with the uneven formation of FeNi spherical structures is evident (Figure 1c,d). This disparity indicates a deviation from the expected morphology, likely attributed to excessive loading of Fe and Ni during the prolonged deposition time. The overloading effect may induce agglomeration and disrupt the desired nanowire formation, leading to irregular and less-defined structures in FeNi-80. The observed morphological differences between FeNi-40 and

https://doi.org/10.1021/acsomega.4c04274
ACS Omega 2024, 9, 42766−42777

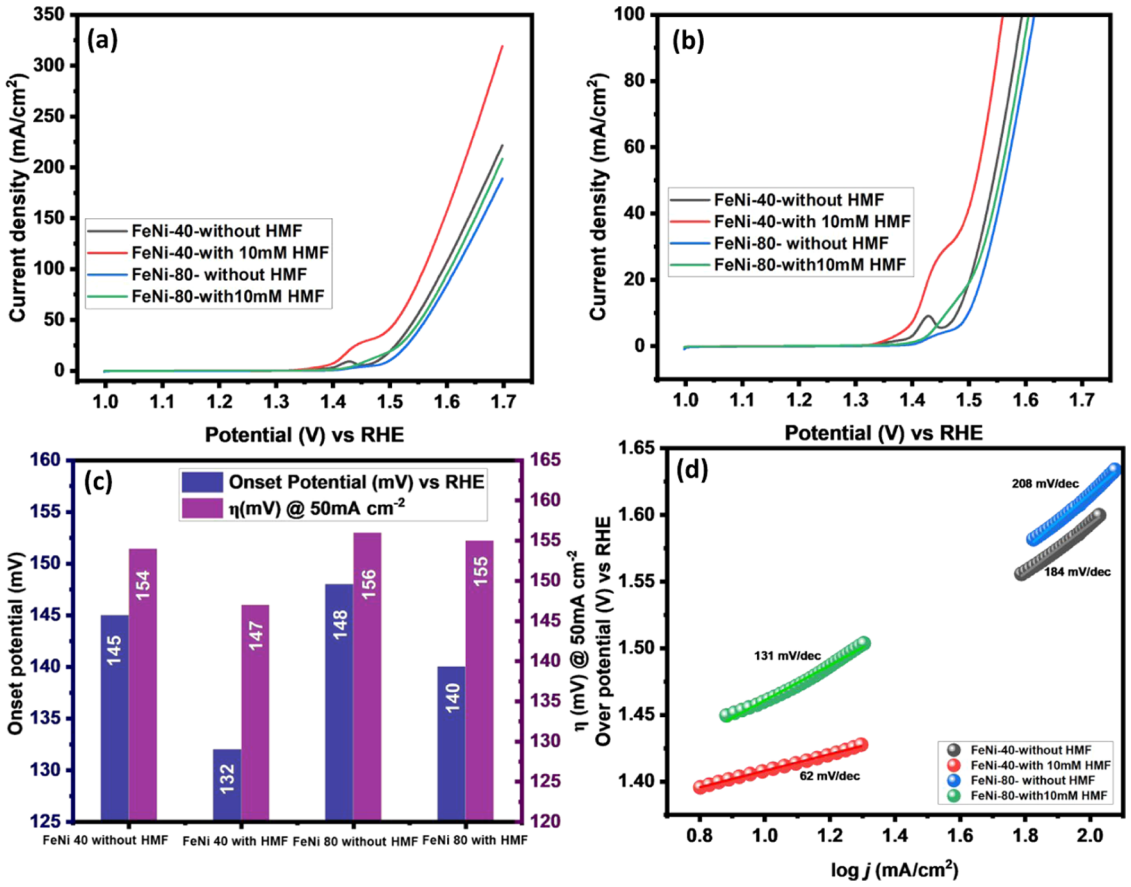

Figure 3. (a) LSV curves of the FeNi-40 and FeNi-80 electrodes, with and without 10 mM HMF, conducted in a 1.0 M KOH electrolyte at a constant scan rate of 5 mV s^{-1}. (b) Magnified images of the LSV curve. (c) Comparison of onset potentials and overpotentials required to achieve a current density of 50 mA cm^{-2} across various electrodes with and without HMF. (d) Corresponding Tafel plots depicting the electrocatalytic behavior of the FeNi-40 and FeNi-80 electrodes illustrate the influence of HMF on reaction kinetics.

FeNi-80 significantly affect catalytic behavior, particularly in the HMFOR reaction.

The energy-dispersive X-ray spectroscopy (EDX) results for FeNi-40 and FeNi-80 provide critical insights into the impact of deposition time on the composition and morphology of the catalysts synthesized via AACVD. FeNi-40, deposited over 40 min, exhibits a nanowire morphology with a relatively balanced composition of 52.4% Fe and 47.6% Ni by atomic weight (Figure S3A,B). This balanced Fe/Ni ratio suggests a well-mixed alloy, likely contributing to the high surface area and increased availability of active sites crucial for catalytic processes. In contrast, EDX analysis of FeNi-80 reveals a higher iron content of 60.8% Fe than 39.2% Ni (Figure S3C,D). The increased iron concentration and the aggregated morphology suggest a possible phase separation or uneven alloying, which could impair the catalyst's efficiency. The higher iron content in FeNi-80 may lead to a denser, less porous material, further limiting the interaction between the catalyst and the reactants. This could explain the observed decrease in catalytic activity for FeNi-80, as the reduced surface area and less homogeneous composition likely hinder effective HMF oxidation.

XRD analysis was performed on the FeNi alloys deposited for different durations, namely, FeNi-40 and FeNi-80, to investigate their crystalline structure and phase composition. Figure 2, the XRD patterns of FeNi-40 and FeNi-80, exhibited prominent reflections at 2θ angles of approximately 44.86, 52.04, and 76.15°. These reflections correspond to the planes (111), (200), and (220) of a face-centered cubic (FCC) crystal structure of FeNi alloys. The observed diffraction reflections agree with the (JCPDS card number-012-0736), confirming the formation of FCC FeNi alloy.[38] The absence of additional reflection in the XRD patterns suggests a high purity and phase homogeneity in both FeNi-40 and FeNi-80 samples. This is further supported by the vigorous intensity of the observed diffraction reflections, indicating well-defined crystalline structures. Interestingly, despite the variation in surface morphology depending on the deposition time between the FeNi-40 and FeNi-80 samples, XRD analysis revealed no difference in crystallinity or crystal phase.

The X-ray photoelectron spectroscopy (XPS) data for the Fe−Ni alloy, as presented in Figure 2b,c, offer significant insights into the chemical composition and oxidation states of the elements involved. The Fe 2p spectrum reveals multiple peaks, including the Fe $2p_{1/2}$ and Fe $2p_{3/2}$ components, alongside characteristic satellite peaks. Notably, the Fe $2p_{3/2}$ peak around 710.62 eV indicates the presence of Fe^{3+} ions, while the corresponding Fe $2p_{1/2}$ peak at approximately 723.7 eV confirms this state. The presence of Fe^{2+} ions is also evident from peaks at similar binding energies, highlighting a mixed-valence state for iron. This mixed oxidation state, often resulting from surface oxidation or air exposure, is crucial. It provides a range of active sites that can enhance catalytic performance, particularly for redox reactions involved in

https://doi.org/10.1021/acsomega.4c04274
ACS Omega 2024, 9, 42766−42777

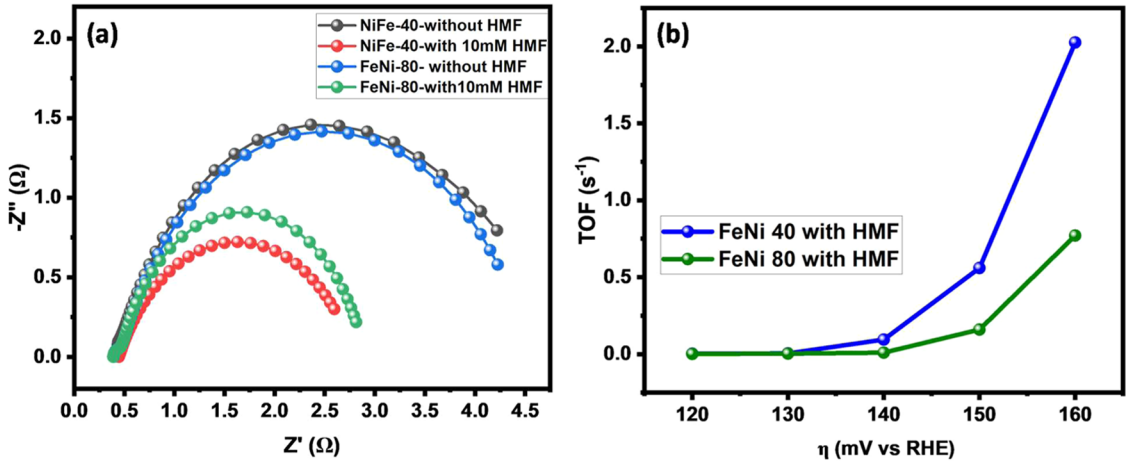

Figure 4. (a) EIS curves illustrating the impedance behavior of the FeNi-40 and FeNi-80 electrodes, both with and without the presence of 10 mM HMF, in a 1.0 M KOH electrolyte. (b) Turnover frequency (TOF) analysis of FeNi-40 and FeNi-80 electrodes under the influence of 10 mM HMF, derived from various potentials along the polarization curve, highlighting the catalytic activity of the alloys.

processes such as HMF oxidation. The Ni 2p spectrum further supports the alloy's composition by displaying a prominent Ni $2p_{3/2}$ peak at around 855.2 eV, indicative of metallic Ni 0. This suggests that a substantial portion of nickel remains unoxidized, preserving the structural and electronic properties necessary for effective catalysis. The satellite peaks associated with Ni^{2+}, observed around 862.9 eV, indicate surface oxidation, forming nickel oxides or hydroxides. The presence of these oxides, while potentially altering the electronic environment of the surface, can also contribute additional active sites for catalytic reactions. Thus, the XPS analysis reveals that the Fe−Ni alloy surface combines oxidized iron, nickel, and metallic nickel.

Electrochemical Analysis of Prepared Catalysts for OER and HMFOR. The electrocatalytic performance of FeNi-40 and FeNi-80 for both the OER and HMFOR was systematically investigated by linear sweep voltammetry (LSV) in a 1.0 M KOH electrolyte using a reference Hg/HgO electrode with a fixed scan rate of 5 mV s^{-1}. As depicted in Figure 3a, the results reveal significant differences in the onset potentials and overpotentials of the two catalysts with and without 10 mM HMF. For FeNi-40, the OER exhibited an onset potential of 1.45 V and an overpotential of 1.54 V vs RHE at a current density of 50 mA cm^{-2}, indicative of its effective catalytic activity for oxygen evolution. After adding 10 mM HMF, FeNi-40 exhibited a reduced onset potential of 1.32 V and a lower overpotential of 1.47 V vs RHE at 50 mA cm^{-2} current density, signifying increased catalytic activity toward HMFOR. The observed decrease in the onset potential and overpotential in the presence of HMF suggests efficient oxidation of HMF in FeNi-40, highlighting its potential as a superior catalyst for biomass conversion.

Interestingly, a peak observed at 1.42 mV in the OER curve (Figure 3b) suggests potential Ni oxidation from Ni^{2+} to Ni^{3+}, a common phenomenon in Ni-based catalysts. However, the addition of HMF indicates that the presence of HMF influences the oxidation behavior, potentially inhibiting the Ni oxidation process. On the contrary, FeNi-80 showed less favorable electrocatalytic activity than FeNi-40 for the OER and HMFOR. FeNi-80 exhibited higher onset potentials of 1.48 V for the OER and 1040 V for the HMFOR and overpotentials, 1.56 V for the OER and 1.55 V for the HMFOR at 50 mA cm^{-2} current density, indicating inferior catalytic performance. This can be attributed to the morphology of FeNi-80, characterized by irregularities and disruptions, which likely reduce the availability of active sites and hinder catalytic efficiency. Figure 3c presents a comparative analysis of the onset and overpotentials at 50 mA cm^{-2} for the OER and HMFOR. Both FeNi-40 and FeNi-80 demonstrate lower onset and overpotentials for HMFOR compared to the OER, indicating the superiority of HMFOR over the OER in terms of catalytic efficiency. In addition, to provide a direct comparison, we normalized the applied potential for HMF oxidation by dividing the current density by the electrochemically active surface area (ECSA) value in Figure S4. The ECSA-normalized current densities were determined at an applied potential of 1.6 V vs RHE. The ECSA-normalized current density for FeNi-40 was found to be 5.2 mA/cm^2, while FeNi-80 exhibited a current density of 4.1 mA/cm^2. This indicates that FeNi-40 still demonstrates superior catalytic activity per unit active surface area compared to FeNi-80.

Tafel plot analysis is a powerful technique for understanding the kinetics and mechanisms of electrochemical reactions. Tafel plots were used to investigate the kinetics of the OER and HMFOR catalyzed by FeNi-40 and FeNi-80 catalysts, both with and without 10 mM of HMF. Figure 3d illustrates the Tafel slope values obtained from the polarization plots. As a result, FeNi-40 with 10 mM HMF exhibited the lowest Tafel slope value of 61 mV/dec, indicating rapid kinetics and efficient catalytic activity for both HMFOR processes. The presence of HMF likely enhances the electrochemical reaction kinetics by facilitating the adsorption and activation of the reactant on the catalyst surface, leading to an improved performance. FeNi-80 with 10 mM HMF exhibits a higher Tafel slope value of 131 mV/dec in comparison to FeNi-40, indicating slower kinetics and less efficient catalysis. This suggests that the morphology and composition of FeNi-80 may not be as conducive to efficient electrocatalytic activity, resulting in decreased performance even in the presence of HMF. When comparing the Tafel slope values of FeNi-40 and FeNi-80 without HMF, FeNi-40 184 mV/dec demonstrates superior catalytic kinetics for the OER compared to FeNi-80 208 mV/dec. This highlights the influence of catalyst composition and morphology on the electrochemical perform-

https://doi.org/10.1021/acsomega.4c04274
ACS Omega 2024, 9, 42766−42777

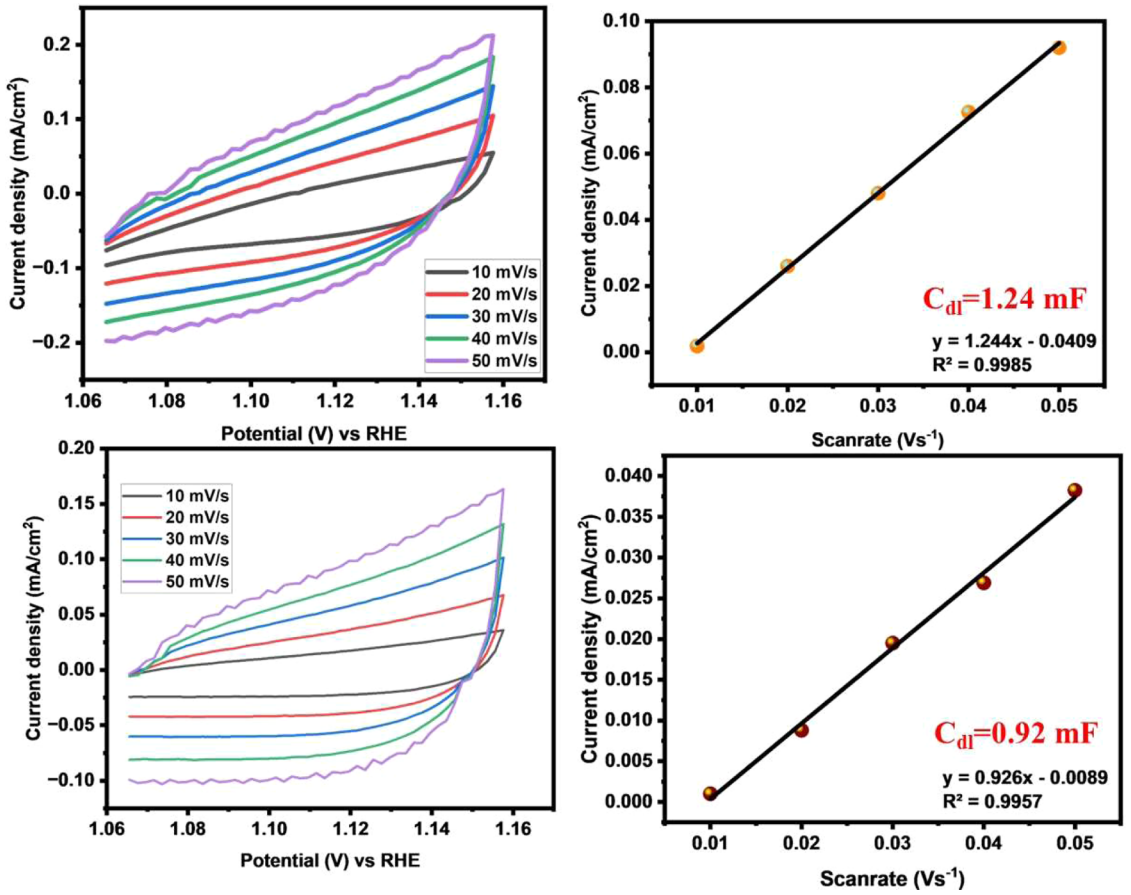

Figure 5. (a and c) Cyclic voltammetry (CV) curves of the FeNi-40 and FeNi-80 electrodes recorded at various scan rates, revealing the electrochemical behavior of the alloys. (b, d) Linear regression plots correlate the current response with the scan rate for the FeNi-40 and FeNi-80 electrodes, facilitating the determination of ECSA from the CV data.

ance, with FeNi-40 exhibiting better activity even without HMF.

Electrochemical Impedance Spectroscopy (EIS) Analysis of Different Catalysts in the Absence and Presence of HMF. Electrochemical impedance spectroscopy (EIS) studies provided additional insights into the electrocatalytic behavior of FeNi-40 and FeNi-80, particularly in 10 mM HMF. Figure 4a illustrates the Nyquist plot for the prepared electrodes at an applied potential of 1.45 V vs RHE with and without 10 mM HMF. The FeNi-40 electrode with 10 mM HMF exhibits the smallest semicircle, indicating the lowest charge transfer resistance among the tested conditions. This suggests that the presence of HMF facilitates charge transfer and enhances the electrochemical activity of the FeNi-40 electrode. The equivalent circuit model fitted to the Nyquist plot provides additional insights into the electrochemical processes at the electrode−electrolyte interface. Supporting Information, Figure S1 discusses the fitted circuit model. The measurement of charge transfer resistance (R_{ct}) is particularly significant because it reflects the ease with which charge is transferred across the electrode−electrolyte interface. A lower R_{ct} value indicates faster charge transfer kinetics and improved electrochemical performance. In this study, FeNi-40 electrodes exhibit lower R_{ct} values in the presence of HMF 2.17 than those without HMF 3.79 Ω, indicating an increased charge transfer efficiency with HMF addition. Similarly, FeNi-80 electrodes also show reduced R_{ct} values with HMF 2.4 Ω compared to those without HMF 3.8.

The turnover frequency (TOF) is a crucial parameter in catalysis, representing the number of catalytic events per active site and per unit time. This study measured the TOF of the as-prepared FeNi-40 and FeNi-80 catalysts in 10 mM HMF to evaluate their catalytic efficiency for HMFOR. The TOF was calculated using eq 2:

$$\mathrm{TOF} = (J \times A)/6 \times F \times m \quad (2)$$

where J is the current density (A/cm^2), F is the Faraday constant (96,485 C/mol), A is the electrode area (1 cm^2), and m is the mass/mol of catalyst deposited on the electrode surface (g/mol). At an overpotential of 1.6 V vs RHE, the TOF of FeNi-40 and FeNi-80 was measured to be 2.03 and 0.78 s^{-1}, respectively. The higher TOF value obtained for FeNi-40 than for FeNi-80 suggests that FeNi-40 exhibits excellent catalytic activity and efficiency for HMFOR in 10 mM HMF. This difference in TOF can be attributed to the more favorable morphology and composition of FeNi-40, which provides a higher density of active sites for HMF oxidation.

Electrochemical Active Surface Area Measurements. The electrochemically active surface area (ECSA) of catalysts is a crucial parameter that directly influences their catalytic performance. This study evaluated the ECSA of FeNi-40 and FeNi-80 catalysts by using cyclic voltammetry (CV) measurements at different scan rates. Figure 5a shows the CV obtained for FeNi-40 at various scan rates. In contrast, Figure 5b shows the linear relationship between the current and scan rate, characteristic of a double-layer capacitance process. Similarly,

https://doi.org/10.1021/acsomega.4c04274
ACS Omega 2024, 9, 42766−42777

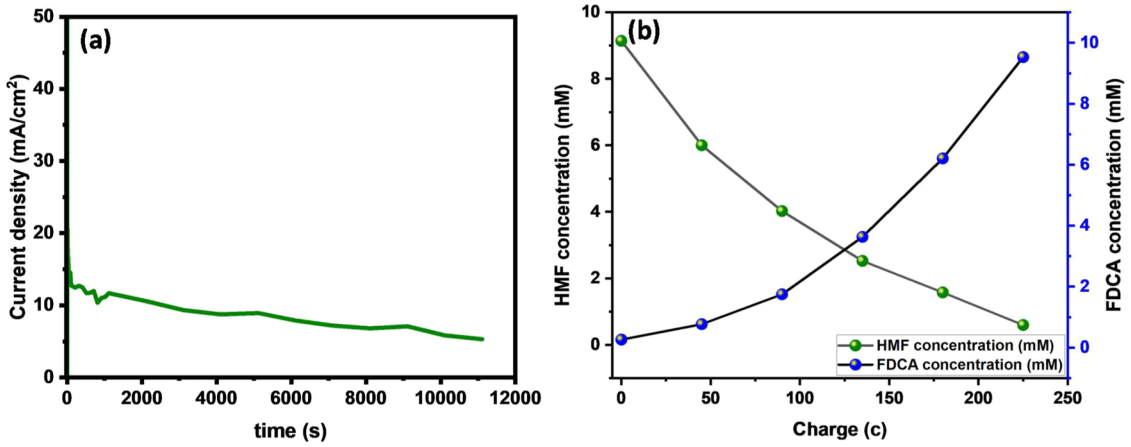

Figure 6. (a) Time-dependent concentration changes of HMF and its oxidation products during CA tests conducted at 1.45 V vs RHE, providing information on the electrochemical conversion process. (b) Relationship between HMF conversion and FDCA formation concentrations is plotted against the charge, revealing the efficiency of HMF oxidation and FDCA synthesis under electrochemical conditions.

Chart 1. Schematic Representation of the General Mechanism Underlying the Oxidation of HMF to FDCA Is a Key Step in Biomass Conversion Processes for Sustainable Chemical Production

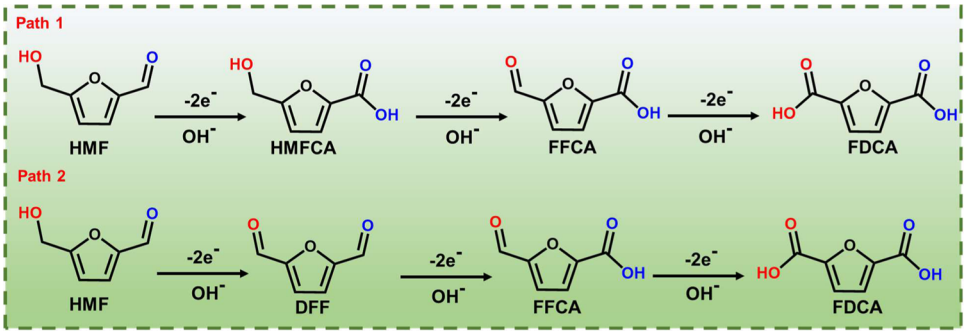

Table 1. Comparative Table of HMFOR Parameters over Prepared Catalysts Compared with Previously Reported Catalysts

electrode	HMF concentration (mM)	oxidation potential (V) vs RHE	FDCA yield (%)	Faradic efficiency	references
$NiCo_2O_4$/NiF	5	1.5	90.4	87.5	40
NiB_x-$P_{0.07}$	10	1.46	90.6	92.5	41
Co_4N@CeO_2	10	1.425	93.6	84.5	42
WO_3/Ni	5	1.37	88.3	88	43
NiO-N/C	10	1.473	84	96	44
Ni@C-250	50	1.45	91	95	45
Co-doped NiCoBDC	10	1.55	99	78.8	46
Pd/VN	10	1.36	88	84	47
NiO-Co_3O_4	10	1.28		96.0	48
NiO-CMK	20	1.85	79	70	49
NF@Mo−$Ni_{0.85}Se$	10	1.40	95	95	50
Ni_3N−V_2O_3	10		98.7		51
FeNi-40	10	1.32	95.3	96.42	this work

Figure 5c,d depict the CV and linear plots for FeNi-80. The slope of the linear plot, which represents the double-layer capacitance (C_{dl}), was measured to be 1.24 mF for FeNi-40 and 0.92 mF for FeNi-80. The double-layer capacitance is directly proportional to the ECSA of the catalyst. The ECSA was calculated using eq 3

$$\text{ECSA} = C_{dl}/C_s \quad (3)$$

where C_s is the specific capacitance of the electrolyte, and C_s is determined to be 0.04 mF.

Substituting the measured values of C_{dl} and C_s into the equation, the ECSA of FeNi-40 and FeNi-80 was calculated to be 31 and 23 cm^2, respectively. The higher ECSA observed for FeNi-40 than FeNi-80 suggests that FeNi-40 possesses a larger active surface area for electrochemical reactions. This larger surface area likely results in a higher density of active sites, leading to enhanced catalytic activity. The observed differences in ECSA between FeNi-40 and FeNi-80 highlight the importance of the morphology and composition of the catalyst in optimizing electrochemical performance.

HMF Conversion and Analysis of Products in FeNi-40/NF. Chronoamperometry (CA) is a powerful technique used to monitor the progress of electrochemical reactions over time by applying a constant potential. In this study, CA was

https://doi.org/10.1021/acsomega.4c04274
ACS Omega 2024, 9, 42766−42777

performed to oxidize 10 mM HMF in 1.0 M KOH electrolyte with a steady potential of 1.45 V vs RHE. Figure 6a shows the CA curves obtained for FeNi-40, which indicate a decrease in current over time, suggesting a reduction in HMF concentration due to oxidation. High-performance liquid chromatography (HPLC) was employed for further quantitative analysis to investigate the product distribution during oxidation. The samples were collected at regular intervals during CA and analyzed using HPLC. The oxidation of HMF typically occurs via two pathways:[39] in Path 1, the aldehyde group in HMF is oxidized to form HMFCA, while in Path 2, the hydroxyl group in HMF is oxidized to form DFF. HMFCA and DFF can further oxidize to form FFCA, and then, FFCA can undergo further oxidation to form FDCA (Chart 1).

The analysis revealed a decrease in HMF concentration over time, accompanied by a parallel increase in FDCA concentration, as depicted in Figure 6b. Intermediate products such as HMFCA and FFCA were also observed, with the concentration of HMFCA initially increasing and then decreasing over time, indicating that HMF conversion occurs predominantly through Path 1. Based on theoretical calculations, the charge consumed during the oxidation process was estimated to be 84.3C. Product analysis and faradic efficiency were measured by using the theoretical formula given in S2. Furthermore, the Faradaic efficiency and product yield were measured at 96.4 and 95.3%, respectively, indicating the high efficiency and selectivity of the electrochemical oxidation process. The observed product distribution and high Faradaic efficiency highlight the potential of FeNi-40 as an efficient catalyst for biomass conversion applications. In addition, Table 1 presents a comparative analysis of the prepared catalyst with other catalysts for the conversion of HMF. As a result, the FeNi-40 catalyst demonstrates exceptional performance for the oxidation of HMF than many other nickel-based and bimetallic catalysts.

Stability of FeNi-40/NF. A chronopotentiometry (CP) test was conducted without HMF to assess the electrode's durability, maintaining an applied current density of 50 mA cm^{-2}. The choice to exclude HMF during this test was driven by the need to isolate the electrode's intrinsic stability without the influence of reactants, which can introduce variable degradation pathways. This approach ensures a clearer understanding of the electrode's resilience under purely electrochemical conditions. As depicted in Figure S5A, the Fe−Ni-40 electrode demonstrated remarkable stability over a duration exceeding 7 h, maintaining a steady potential around 1.5 V vs RHE. This stability suggests that the electrode's structural integrity and catalytic sites remain intact under prolonged electrochemical stress, which is crucial for real-world applications where long-term operation without performance degradation is essential. Subsequently, the long-term stability of the Fe−Ni-40 electrode was evaluated in the presence of 10 mM HMF under optimized conditions, reflecting a more realistic operational scenario where the electrode is exposed to reactants and potential byproducts. This evaluation involved intermittent usage over 15 days, during which the electrode was stored in an airtight container when not in use to prevent environmental degradation or contamination. The results, summarized in Figure S5B, reveal that the electrode retained 92.06% of its initial current response after 15 days, a testament to its robust stability and resilience. This slight decrease in the current response can be attributed to minor surface passivation or fouling, common in electrocatalytic processes involving organic substrates. This high retention highlights the electrode's resilience and suitability for prolonged use in catalytic applications, emphasizing its potential for sustainable energy and chemical production processes.

The FeNi-40/NF catalyst's stability before and after the HMF oxidation reaction was further evaluated through XRD analysis. Following the HMFOR process, in Figure 7, the XRD

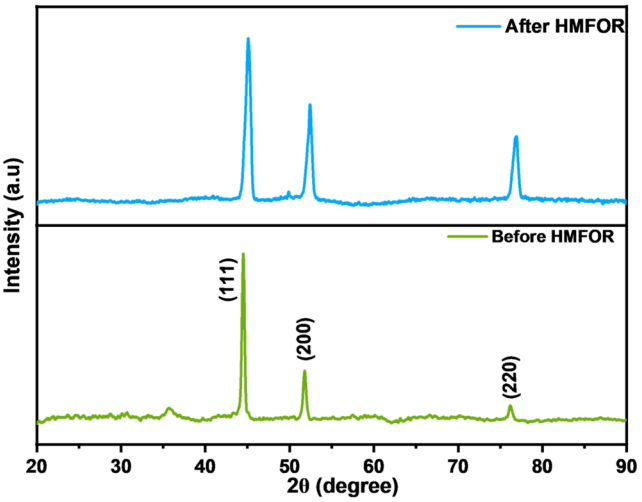

Figure 7. XRD patterns of the FeNi-40/NF catalyst before and after HMFOR.

patterns continue to show reflections at similar 2θ angles, indicating the retention of the FCC structure. However, a slight shift in peak positions toward lower 2θ angles of 52.04° (52.29°) and 76.15° (76.68°) is observed. This could be due to incorporating HMF oxidation products or absorbed species into the crystal lattice, causing lattice expansion. Moreover, the absence of additional peaks in the XRD pattern post-HMFOR indicates that no new crystalline phases or any phase transformations were formed during the electrochemical reaction. Finally, this postcharacterization of XRD results suggests that the FeNi alloy is robust and capable of retaining its catalytic properties under electrochemical conditions. This resilience makes it a promising electrode for long-term use in electrochemical processes of HMF oxidation.

CONCLUSIONS

This study investigated the AACVD-based synthesis of FeNi alloy nanostructures with different morphologies. It explored their electrochemical performance in oxidizing biomass-derived HMF to FDCA, an organic molecule used as an intermediate for many industrially viable fine chemicals. Morphological analysis revealed that FeNi alloy nanowires synthesized for a short reaction time (FeNi-40) exhibited superior catalytic efficiency compared with the FeNi alloy (FeNi-80), which displayed irregular nanostructures. X-ray diffraction (XRD) analysis confirmed the successful formation of FeNi alloys with a FCC crystal structure. Electrochemical characterization demonstrated that FeNi-40 exhibited onset potentials of 1.32 V versus RHE for HMF oxidation lower than those of FeNi-80, indicating superior catalytic activity. Tafel plot analysis further confirmed the enhanced kinetics of HMF oxidation on FeNi-40, attributed to its lower resistance to charge transfer. The investigation of ECSA revealed a larger

https://doi.org/10.1021/acsomega.4c04274
ACS Omega 2024, 9, 42766−42777

ECSA for FeNi-40 compared with FeNi-80, indicating a higher density of active sites for electrochemical reactions. CA analysis combined with HPLC's product analysis demonstrated efficient HMF oxidation in FeNi-40, with a high product yield (95.3%) and Faradaic efficiency (96.42%). In addition, the results of this study provide valuable insight into the electrochemical performance of FeNi catalysts for biomass conversion and lay the foundation for future research to advance sustainable catalysis for renewable energy and chemical production.

■ ASSOCIATED CONTENT

Supporting Information

The Supporting Information is available free of charge at https://pubs.acs.org/doi/10.1021/acsomega.4c04274.

EIS fitting model; product analysis; randles cell model equivalent circuit (Figure S1); calibration of the HPLC for (a) HMF, (b) FDCA, and HMFCA (c) (Figure S2); (A) SEM image of FeNi-40 nanostructures, synthesized with a deposition time of 40 min, showing a dense network of nanowires (Figure S3); ECSA-normalized LSV Curves of FeNi-40 and FeNi-80 for HMF oxidation (Figure S4); (A) chronopotentiometry (CP) test of the Fe−Ni-40 electrode at 50 mA cm^{-2} without HMF, showing stable performance over 7 h (Figure S5) (PDF)

■ AUTHOR INFORMATION

Corresponding Author

Wasif Farooq − *Interdisciplinary Research Centre for Refining and Advanced Chemicals (IRC-RAC), King Fahd University of Petroleum & Minerals, Dhahran 31261, Kingdom of Saudi Arabia; Department of Chemical Engineering, King Fahd University of Petroleum & Minerals, Dhahran 31261, Kingdom of Saudi Arabia;* orcid.org/0000-0002-4882-0097; Email: wasif@kfupm.edu.sa

Authors

Muthumariappan Akilarasan − *Interdisciplinary Research Centre for Refining and Advanced Chemicals (IRC-RAC), King Fahd University of Petroleum & Minerals, Dhahran 31261, Kingdom of Saudi Arabia;* orcid.org/0000-0001-8344-4181

Muhammad Ali Ehsan − *Interdisciplinary Research Center for Hydrogen Technologies and Carbon Management (IRC-HTCM), King Fahd University of Petroleum & Minerals, Dhahran 31261, Kingdom of Saudi Arabia;* orcid.org/0000-0002-9780-4042

Muhammad Nawaz Tahir − *Interdisciplinary Research Center for Hydrogen Technologies and Carbon Management (IRC-HTCM) and Chemistry Department, King Fahd University of Petroleum & Minerals, Dhahran 31261, Kingdom of Saudi Arabia;* orcid.org/0000-0002-9031-5537

Mudasir Akbar Shah − *Department of Chemical Engineering, King Fahd University of Petroleum & Minerals, Dhahran 31261, Kingdom of Saudi Arabia*

Jerome Morris Princey − *PG&Research Department of Chemistry, Holy Cross College (Autonomous), Tiruchirappalli, Tamil Nadu 620002, India*

Complete contact information is available at: https://pubs.acs.org/10.1021/acsomega.4c04274

Author Contributions

M.A.: Conceptualization, methodology, data curation, writing-original draft, and review & editing. M.A.E.: Catalyst physical characterization, data curation, writing-original draft, and review & editing. M.N.T.: Formal analysis, validation, and supervision. M.A.S.: Conceptualization and data curation. W.F.: Writing, review & editing, validation, supervision, project administration, and funding acquisition. J.M.P.: Software and formal analysis.

Notes

The authors declare no competing financial interest.

■ ACKNOWLEDGMENTS

The authors thank the Chemical Engineering Department and Interdisciplinary Research Centre for Refining & Advanced Chemicals (IRC-RAC), King Fahd University of Petroleum and Minerals, Saudi Arabia. Furthermore, this work was supported by the funding from Deanship of Research, Oversight, and Coordination (DROC), King Fahd University of Petroleum and Minerals (KFUPM), Saudi Arabia, under the project number (DF191040).

■ REFERENCES

(1) Nawaz, G.; Fatima, M.; Ahmad, Z.; Saleem Joya, K.; Ali Assiri, M.; Imran Abbas Shah, S.; Yasmeen, F.; Naeem Khan, M. Highly Selective and Effective Oxidation of 5-Hydroxymethylfurfural by Co-Ni Based Electrodeposited Bimetallic Oxide Nanostructures. *Fuel* **2024**, *362*, No. 130828.

(2) Kubota, S. R.; Choi, K. Electrochemical Oxidation of 5-Hydroxymethylfurfural to 2,5-Furandicarboxylic Acid (FDCA) in Acidic Media Enabling Spontaneous FDCA Separation. *ChemSusChem* **2018**, *11* (13), 2138−2145.

(3) Caes, B. R.; Teixeira, R. E.; Knapp, K. G.; Raines, R. T. Biomass to Furanics: Renewable Routes to Chemicals and Fuels. *ACS Sustainable Chem. Eng.* **2015**, *3* (11), 2591−2605.

(4) Ashraf, M.; Ullah, N.; Khan, I.; Tremel, W.; Ahmad, S.; Tahir, M. N. Photoreforming of Waste Polymers for Sustainable Hydrogen Fuel and Chemicals Feedstock: Waste to Energy. *Chem. Rev.* **2023**, *123* (8), 4443−4509.

(5) Ashraf, M.; Ayaz, M.; Khan, M.; Adil, S. F.; Farooq, W.; Ullah, N.; Nawaz Tahir, M. Recent Trends in Sustainable Solar Energy Conversion Technologies: Mechanisms, Prospects, and Challenges. *Energy Fuels* **2023**, *37* (9), 6283−6301.

(6) Li, Z.; Han, Y.; Huang, B.; Xie, Z.; Wei, Q.-H. Electrochemical oxidation of 5-Hydroxymethylfurfural over a Molybdenum Sulfide Modified Nickel-Based Catalyst. *Mater. Adv.* **2023**, *4* (11), 2449−2456.

(7) Zhang, L.; Liu, Z.; Cui, G.; Chen, L. Biomass-Derived Materials for Electrochemical Energy Storages. *Prog. Polym. Sci.* **2015**, *43*, 136−164.

(8) Chen, Z.; Liao, S.; Ge, L.; Amaniampong, P. N.; Min, Y.; Wang, C.; Li, K.; Lee, J.-M. Reduced Graphene Oxide with Controllably Intimate Bifunctionality for the Catalytic Transformation of Fructose into 2,5-Diformylfuran in Biphasic Solvent Systems. *Chem. Eng. J.* **2020**, *379*, No. 122284.

(9) Gao, T.; Chen, J.; Fang, W.; Cao, Q.; Su, W.; Dumeignil, F. Ru/Mn Ce1O Catalysts with Enhanced Oxygen Mobility and Strong Metal-Support Interaction: Exceptional Performances in 5-Hydroxymethylfurfural Base-Free Aerobic Oxidation. *J. Catal.* **2018**, *368*, 53−68.

(10) Xu, S.; Zhou, P.; Zhang, Z.; Yang, C.; Zhang, B.; Deng, K.; Bottle, S.; Zhu, H. Selective Oxidation of 5-Hydroxymethylfurfural to 2,5-Furandicarboxylic Acid Using O_2 and a Photocatalyst of Co-Thioporphyrazine Bonded to g-C_3N_4. *J. Am. Chem. Soc.* **2017**, *139* (41), 14775−14782.

(11) Chen, G.; Wu, L.; Fan, H.; Li, B. Highly Efficient Two-Step Synthesis of 2,5-Furandicarboxylic Acid from Fructose without 5-Hydroxymethylfurfural (HMF) Separation: In Situ Oxidation of HMF in Alkaline Aqueous H_2O/DMSO Mixed Solvent under Mild Conditions. *Ind. Eng. Chem. Res.* **2018**, *57* (48), 16172−16181.
(12) Chu, S.; Cui, Y.; Liu, N. The Path towards Sustainable Energy. *Nat. Mater.* **2017**, *16* (1), 16−22.
(13) Sobota, L.; Bondue, C. J.; Hosseini, P.; Kaiser, C.; Spallek, M.; Tschulik, K. Impact of the Electrochemically Inert Furan Ring on the Oxidation of the Alcohol and Aldehyde Functional Group of 5-Hydroxymethylfurfural (HMF). *ChemElectroChem* **2024**, *11* (1), No. e202300151, DOI: 10.1002/celc.202300151.
(14) MariaJoseph, A.; Nangan, S.; Verma, D.; Gnanasekaran, L.; Rajendran, S.; Natesan, T.; Pattananuwat, P.; Okhawilai, M. Rational Coupling of Selective Electrochemical Oxidation and Reduction Reactions for In-Situ Value-Added Chemical Generation. *Fuel* **2024**, *367*, No. 131408.
(15) Akilarasan, M.; Tamilalagan, E.; Chen, S.-M. Synthesis of Pyrochlore-Type La2Sn2O7@GO for the in-Situ Profiling of Organophosphate Pesticides Paraoxon Ethyl in Environmental Samples. *J. Environ. Chem. Eng.* **2024**, *12* (2), No. 111928.
(16) Sriram, B.; Kogularasu, S.; Wang, S.-F.; Sheu, J.-K. Deep Eutectic Solvent-Mediated Synthesis of Spinel Zinc Chromite Nanoparticles: A Simple Label-Free Electrochemical Sensor for Dopamine and Ascorbic Acid. *ACS Appl. Nano Mater.* **2023**, *6* (19), 17593−17602.
(17) Yang, Y.; Mu, T. Electrochemical Oxidation of Biomass Derived 5-Hydroxymethylfurfural (HMF): Pathway, Mechanism, Catalysts and Coupling Reactions. *Green Chem.* **2021**, *23* (12), 4228−4254.
(18) Zhang, M.; Liu, Y.; Liu, B.; Chen, Z.; Xu, H.; Yan, K. Trimetallic NiCoFe-Layered Double Hydroxides Nanosheets Efficient for Oxygen Evolution and Highly Selective Oxidation of Biomass-Derived 5-Hydroxymethylfurfural. *ACS Catal.* **2020**, *10* (9), 5179−5189.
(19) Liu, B.; Xu, S.; Zhang, M.; Li, X.; Decarolis, D.; Liu, Y.; Wang, Y.; Gibson, E. K.; Catlow, C. R. A.; Yan, K. Electrochemical Upgrading of Biomass-Derived 5-Hydroxymethylfurfural and Furfural over Oxygen Vacancy-Rich NiCoMn-Layered Double Hydroxides Nanosheets. *Green Chem.* **2021**, *23* (11), 4034−4043.
(20) You, B.; Jiang, N.; Liu, X.; Sun, Y. Simultaneous H_2 Generation and Biomass Upgrading in Water by an Efficient Noble-Metal-Free Bifunctional Electrocatalyst. *Angew. Chem., Int. Ed.* **2016**, *55* (34), 9913−9917.
(21) Wang, J.; Zhao, W.; Yu, H.; Wang, W.; Xu, Y.; Shen, L.-L.; Zhang, G.-R.; Mei, D. Enhanced Electrochemical Oxidation of 5-Hydroxymethylfurfural over Tailored Nickel Nanoparticle Assembly. *Appl. Catal., B* **2024**, *353*, No. 124086.
(22) Ge, R.; Wang, Y.; Li, Z.; Xu, M.; Xu, S.; Zhou, H.; Ji, K.; Chen, F.; Zhou, J.; Duan, H. Selective Electrooxidation of Biomass-Derived Alcohols to Aldehydes in a Neutral Medium: Promoted Water Dissociation over a Nickel-Oxide-Supported Ruthenium Single-Atom Catalyst. *Angew. Chem., Int. Ed.* **2022**, *61* (19), No. e202200211, DOI: 10.1002/anie.202200211.
(23) Zheng, R.; Zhao, C.; Xiong, J.; Teng, X.; Chen, W.; Hu, Z.; Chen, Z. Construction of a Hierarchically Structured, NiCo−Cu-Based Trifunctional Electrocatalyst for Efficient Overall Water Splitting and 5-Hydroxymethylfurfural Oxidation. *Sustainable Energy Fuels* **2021**, *5* (16), 4023−4031.
(24) Luo, Y.; Zhang, D.; He, Y.; Zhang, W.; Liu, S.; Zhu, K.; Huang, L.; Yang, Y.; Wang, G.; Yu, R.; Shu, H.; Wang, X.; Chen, M. Intergrated Morphology Engineering and Alloying Strategy for FeNi@NC Catalysts: Tackling the Polysulfide Shuttle in Li-S Batteries. *Chem. Eng. J.* **2023**, *474*, No. 145751.
(25) Gu, X.; Liu, Z.; Li, M.; Tian, J.; Feng, L. Surface Structure Regulation and Evaluation of FeNi-Based Nanoparticles for Oxygen Evolution Reaction. *Appl. Catal., B* **2021**, *297*, No. 120462.
(26) Zhang, X.; Li, C.; Si, T.; Lei, H.; Wei, C.; Sun, Y.; Zhan, T.; Liu, Q.; Guo, J. FeNi Cubic Cage@N-Doped Carbon Coupled with N-Doped Graphene toward Efficient Electrochemical Water Oxidation. *ACS Sustainable Chem. Eng.* **2018**, *6* (7), 8266−8273.
(27) Yin, Z.; He, R.; Zhang, Y.; Feng, L.; Wu, X.; Wågberg, T.; Hu, G. Electrochemical Deposited Amorphous FeNi Hydroxide Electrode for Oxygen Evolution Reaction. *J. Energy Chem.* **2022**, *69*, 585−592.
(28) Cao, Z.; Zhou, T.; Ma, X.; Shen, Y.; Deng, Q.; Zhang, W.; Zhao, Y. Hydrogen Production from Urea Sewage on NiFe-Based Porous Electrocatalysts. *ACS Sustainable Chem. Eng.* **2020**, *8*, 11007−11015, DOI: 10.1021/acssuschemeng.0c04049.
(29) Gao, D.; Han, F.; Waterhouse, G. I. N.; Li, Y.; Zhang, L. NiFe Layered Double Hydroxide-Derived Catalysts with Remarkable Selectivity for the oxidation of 5-Hydroxymethylfurfural to 2,5-Furanedicarboxylic Acid under Base-Free Conditions. *ACS Sustainable Chem. Eng.* **2023**, *11* (4), 1557−1568.
(30) Jiang, S.; Zhu, L.; Yang, Z.; Wang, Y. Morphological-Modulated FeNi-Based Amorphous Alloys as Efficient Alkaline Water Splitting Electrocatalysts. *Electrochim. Acta* **2021**, *389*, No. 138756.
(31) Muthumariappan, A.; Sakthivel, K.; Chen, S.-M.; Chen, T.-W.; Mani, G.; Lou, B.-S. Effects of Annealing Temperature on Crystal Structure and Glucose Sensing Properties of Cuprous Oxide. *Sens. Actuators, B* **2018**, *266*, 655−663.
(32) Cheng, L.; Wang, Q.; Ding, J. One-step Hydrothermal Synthesis of the $FeNi_3$/RGO Composite for Electrochemical Supercapacitor. *J. Mater. Sci.: Mater. Electron.* **2021**, *32* (6), 7226−7236.
(33) Wang, H.; Tang, J.; Li, Y.; Chu, H.; Ge, Y.; Baines, R.; Dong, P.; Ajayan, P. M.; Shen, J.; Ye, M. Template-Free Solvothermal Preparation of Ternary $FeNi_2S_4$ Hollow Balloons as RuO_2-like Efficient Electrocatalysts for the Oxygen Evolution Reaction with Superior Stability. *J. Mater. Chem. A* **2018**, *6* (40), 19417−19424.
(34) Sharma, S.; Dwivedi, S. P.; Li, C.; Awwad, F. A.; Khan, M. I.; Ismail, E. A. A. Unveiling of Grain Structure, Porosity, Phase Distributions, Microstructural Morphology, Surface Hardness, and Tribo-Corrosion Characteristics of Nickel, and Titanium Dioxide-Based SS-304 Steel Microwave Composite Coatings Cladding. *J. Mater. Res. Technol.* **2024**, *28*, 4299−4316.
(35) Huang, C.-C.; Pourzolfaghar, H.; Huang, C.-L.; Liao, C.-P.; Li, Y.-Y. FeNi Nanoalloy-Carbon Nanotubes on Defected Graphene as an Excellent Electrocatalyst for Lithium-Oxygen Batteries. *Carbon* **2024**, *222*, No. 118973.
(36) Mokrushin, A. S.; Gorban, Y. M.; Averin, A. A.; Gorobtsov, P. Yu.; Simonenko, N. P.; Simonenko, E. P.; Kuznetsov, N. T. Gas Sensing Properties of AACVD-Derived ZnO/Co_3O_4 Bilayer Thin Film Nanocomposites. *Ceram. Int.* **2024**, *50* (6), 8777−8789.
(37) Ehsan, M. A.; Khan, A.; Al-Ahmed, A.; Hakeem, A. S.; Afzaal, M.; Pandey, S.; Mahar, N. Aerosol-Assisted Chemical Vapour Deposited Vanadium Oxide Thin Films on Nickel Foam with Auspicious Electrochemical Water Oxidation Properties. *Int. J. Hydrogen Energy* **2024**, *52*, 718−727.
(38) Dhawale, S. C.; Munde, A. V.; Mulik, B. B.; Dighole, R. P.; Zade, S. S.; Sathe, B. R. CTAB-Assisted Synthesis of FeNi Alloy Nanoparticles: Effective and Stable Electrocatalysts for Urea Oxidation Reactions. *Langmuir* **2024**, *40* (5), 2672−2685.
(39) Zhang, N.; Zou, Y.; Tao, L.; Chen, W.; Zhou, L.; Liu, Z.; Zhou, B.; Huang, G.; Lin, H.; Wang, S. Electrochemical Oxidation of 5-Hydroxymethylfurfural on Nickel Nitride/Carbon Nanosheets: Reaction Pathway Determined by In Situ Sum Frequency Generation Vibrational Spectroscopy. *Angew. Chem., Int. Ed.* **2019**, *58* (44), 15895−15903.
(40) Kang, M. J.; Park, H.; Jegal, J.; Hwang, S. Y.; Kang, Y. S.; Cha, H. G. Electrocatalysis of 5-Hydroxymethylfurfural at Cobalt Based Spinel Catalysts with Filamentous Nanoarchitecture in Alkaline Media. *Appl. Catal., B* **2019**, *242*, 85−91.
(41) Song, X.; Liu, X.; Wang, H.; Guo, Y.; Wang, Y. Improved Performance of Nickel Boride by Phosphorus Doping as an Efficient Electrocatalyst for the oxidation of 5-Hydroxymethylfurfural to 2,5-Furandicarboxylic Acid. *Ind. Eng. Chem. Res.* **2020**, *59* (39), 17348−17356.

(42) Zhou, P.; Hai, G.; Zhao, G.; Li, R.; Huang, X.; Lu, Y.; Wang, G. CeO_2 as an "Electron Pump" to Boost the Performance of Co_4N in Electrocatalytic Hydrogen Evolution, Oxygen Evolution and Biomass Oxidation Valorization. *Appl. Catal., B* **2023**, *325*, No. 122364.
(43) Hu, K.; Zhang, M.; Liu, B.; Yang, Z.; Li, R.; Yan, K. Efficient Electrochemical Oxidation of 5-Hydroxymethylfurfural to 2,5-Furandicarboxylic Acid Using the Facilely Synthesized 3D Porous WO_3/Ni Electrode. *Mol. Catal.* **2021**, *504*, No. 111459.
(44) Wang, W.; Zhang, Z.; Wang, M. Preparation of NiO-N/C Composites for Electrochemical Oxidation of 5-Hydroxymethylfurfural to 2,5-Furandicarboxylic Acid. *Biomass Convers. Biorefin.* **2023**, *13* (18), 17247−17254.
(45) Wang, J.; Zhao, Z.; Shen, C.; Liu, H.; Pang, X.; Gao, M.; Mu, J.; Cao, F.; Li, G. Ni/NiO Heterostructures Encapsulated in Oxygen-Doped Graphene as Multifunctional Electrocatalysts for the HER, UOR and HMF Oxidation Reaction. *Catal. Sci. Technol.* **2021**, *11* (7), 2480−2490.
(46) Cai, M.; Zhang, Y.; Zhao, Y.; Liu, Q.; Li, Y.; Li, G. Two-Dimensional Metal−Organic Framework Nanosheets for Highly Efficient Electrocatalytic Biomass 5-(Hydroxymethyl)Furfural (HMF) Valorization. *J. Mater. Chem. A* **2020**, *8* (39), 20386−20392.
(47) Li, S.; Sun, X.; Yao, Z.; Zhong, X.; Cao, Y.; Liang, Y.; Wei, Z.; Deng, S.; Zhuang, G.; Li, X.; Wang, J. Biomass Valorization via Paired Electrosynthesis Over Vanadium Nitride-Based Electrocatalysts. *Adv. Funct Mater.* **2019**, *29* (42), No. 1904780, DOI: 10.1002/adfm.201904780.
(48) Lu, Y.; Dong, C.-L.; Huang, Y.-C.; Zou, Y.; Liu, Y.; Li, Y.; Zhang, N.; Chen, W.; Zhou, L.; Lin, H.; Wang, S. Hierarchically Nanostructured NiO-Co_3O_4 with Rich Interface Defects for the Electro-Oxidation of 5-Hydroxymethylfurfural. *Sci. China Chem.* **2020**, *63* (7), 980−986.
(49) Holzhäuser, F. J.; Janke, T.; Öztas, F.; Broicher, C.; Palkovits, R. Electrocatalytic oxidation of 5-Hydroxymethylfurfural into the Monomer 2,5-Furandicarboxylic Acid Using Mesostructured Nickel Oxide. *Adv. Sustainable Syst.* **2020**, *4* (10), No. 1900151, DOI: 10.1002/adsu.201900151.
(50) Yang, C.; Wang, C.; Zhou, L.; Duan, W.; Song, Y.; Zhang, F.; Zhen, Y.; Zhang, J.; Bao, W.; Lu, Y.; Wang, D.; Fu, F. Refining D-Band Center in Ni0.85Se by Mo Doping: A Strategy for Boosting Hydrogen Generation via Coupling Electrocatalytic Oxidation 5-Hydroxymethylfurfural. *Chem. Eng. J.* **2021**, *422*, No. 130125.
(51) Liang, S.; Pan, L.; Thomas, T.; Zhu, B.; Chen, C.; Zhang, J.; Shen, H.; Liu, J.; Yang, M. Ni_3N-V_2O_3 Enables Highly Efficient 5-(Hydroxymethyl) Furfural Oxidation Enabling Membrane Free Hydrogen Production. *Chem. Eng. J.* **2021**, *415*, No. 128864, DOI: 10.1016/j.cej.2021.128864.

https://doi.org/10.1021/acsomega.4c04274
ACS Omega 2024, 9, 42766−42777